JACC: BASIC TO TRANSLATIONAL SCIENCE VOL. 8, NO. 5, 2023

ORIGINAL RESEARCH - NOVEL TRANSLATIONAL METHODS

Continuous Monitoring of Blood Pressure and Vascular Hemodynamic Properties With Miniature Extravascular Hall-Based Magnetic Sensor

Konstantinos Magkoutas, MSc,[a] Miriam Weisskopf, DVM,[b] Volkmar Falk, MD,[c,d,e] Maximilian Y. Emmert, MD, PhD,[c,d,f] Mirko Meboldt, PhD,[a] Nikola Cesarovic, DVM, PhD,[c,e,*] Marianne Schmid Daners, PhD[g,*]

VISUAL ABSTRACT

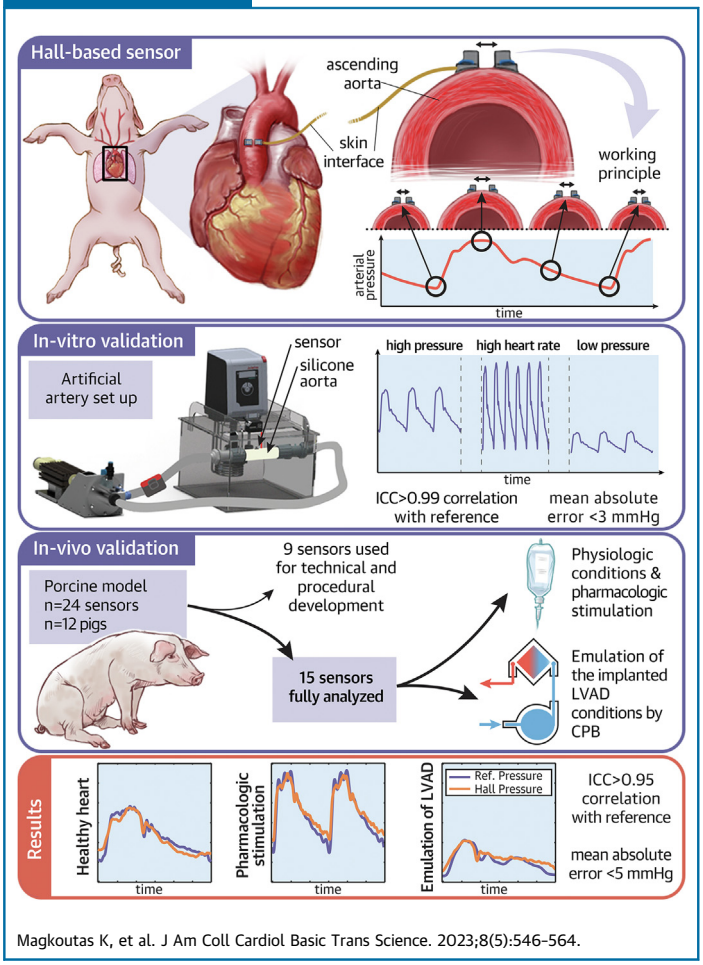

Magkoutas K, et al. J Am Coll Cardiol Basic Trans Science. 2023;8(5):546-564.

HIGHLIGHTS

- **The proposed extravascular hall-based magnetic sensor eliminates the elastic interconnection between the sensing components, avoiding vascular restriction and unwanted sensor-drift phenomena due to material fatigue, while its extra-vascular nature diminishes the risk of thrombosis.**
- **The sensing device has been validated in vivo, in a porcine model under physiologic and pathologic conditions, including cardiopulmonary support.**
- **The sensing device demonstrated unaffected performance after sterilization, immersion in liquid, and temperature changes, while it was able to accurately capture the ABP, with the MAE compared with reference being below 5 mm Hg, even for heart failure conditions, simulated with low blood pulsatility and cardiopulmonary support.**
- **The proposed device may serve as a novel tool for continuous blood pressure monitoring.**

ISSN 2452-302X https://doi.org/10.1016/j.jacbts.2022.12.008

SUMMARY

Continuous measurement of vascular and hemodynamic parameters could improve monitoring of disease progression and enable timely clinical decision making and therapy surveillance in patients suffering from cardiovascular diseases. However, no reliable extravascular implantable sensor technology is currently available. Here, we report the design, characterization, and validation of an extravascular, magnetic flux sensing device capable of capturing the waveforms of the arterial wall diameter, arterial circumferential strain, and arterial pressure without restricting the arterial wall. The implantable sensing device, comprising a magnet and a magnetic flux sensing assembly, both encapsulated in biocompatible structures, has shown to be robust, with temperature and cyclic-loading stability. Continuous and accurate monitoring of arterial blood pressure and vascular properties was demonstrated with the proposed sensor in vitro with a silicone artery model and validated in vivo in a porcine model mimicking physiologic and pathologic hemodynamic conditions. The captured waveforms were further used to deduce the respiration frequency, the duration of the cardiac systolic phase, and the pulse wave velocity. The findings of this study not only suggest that the proposed sensing technology is a promising platform for accurate monitoring of arterial blood pressure and vascular properties, but also highlight the necessary changes in the technology and the implantation procedure to allow the translation of the sensing device in the clinical setting. (J Am Coll Cardiol Basic Trans Science 2023;8:546–564)

ABBREVIATIONS AND ACRONYMS

ABP = arterial blood pressure
ACS = arterial circumferential strain
AD = arterial wall diameter
CPB = cardiopulmonary bypass
CVD = cardiovascular disease
EDP = end-diastolic pressure
HBSD = hall-based sensing device
ICC = intraclass correlation coefficient
MAE = mean absolute error
MAP = mean arterial pressure
PWV = pulse wave velocity
SP = systolic pressure

Cardiovascular diseases (CVDs) affect a large proportion of the Western population and constitute the dominant cause of mortality, accounting for more than 17 million deaths worldwide on a yearly basis.[1] In this context, continuous, long-term monitoring of arterial blood pressure (ABP) and properties that reflect changes in the vascular system can provide useful information on disease progression and enable surveillance of patient compliance and assessment of treatment efficacy.[2-4]

Over the last years, the advent and rapid evolution of stretchable electronics enabled the development of devices that accurately monitor vascular biomechanical properties.[5-8] These properties include pulse wave velocity as well as arterial compliance, distensibility, strain, stress, stiffness, and elasticity.[9-11] However, the most valuable and most easily derived variable that reflects the changes in the overall cardiovascular system is the ABP.[2,12] The waveform of the ABP is affected by left ventricular stroke volume, the biomechanical properties of the aorta, as well as the compliance and resistance of the entire vascular system. Hence, various underlying CVDs alter the ABP waveform (**Figures 1A and 1B**), the analysis of which provides remarkable insights into the dynamic cardiovascular status.[13]

The gold standard method for monitoring ABP is through invasive arterial catheterization, typically using the radial or femoral artery.[14] Although this method enables accurate acquisition of the entire ABP waveform, it cannot be applied long term or in an ambulatory setting. Invasive ABP measurement limits mobilization, bears a risk of vascular thrombosis with downstream occlusion, and is associated with infections and bleeding complications at the access site.[15] To overcome these limitations, new invasive approaches have been investigated that exploit the arterial distension and properties of stretchable electronics to provide monitoring of the ABP.[16-20] While these sensing approaches offer accurate

From the [a]Product Development Group Zurich, Department of Mechanical and Process Engineering, ETH Zurich, Zurich, Switzerland; [b]Center for Surgical Research, University Hospital Zurich, University of Zurich, Zurich, Switzerland; [c]Department of Cardiothoracic and Vascular Surgery, Deutsches Herzzentrum der Charité (DHZC), Berlin, Germany; [d]Charité – Universitätsmedizin Berlin, corporate member of Freie Universität Berlin, Humboldt-Universität zu Berlin, and Berlin Institute of Health, Berlin, Germany; [e]Translational Cardiovascular Technologies, Department of Health Sciences and Technology, ETH Zurich, Zurich, Switzerland; [f]Institute for Regenerative Medicine, University of Zurich, Zurich, Switzerland; and the [g]Institute for Dynamic Systems and Control, Department of Mechanical and Process Engineering, ETH Zurich, Zurich, Switzerland. *Drs Cesarovic and Schmid Daners contributed equally to this work.

The authors attest they are in compliance with human studies committees and animal welfare regulations of the authors' institutions and Food and Drug Administration guidelines, including patient consent where appropriate. For more information, visit the Author Center.

Manuscript received November 8, 2022; revised manuscript received December 29, 2022, accepted December 29, 2022.

FIGURE 1 Sensing Approach of the Hall-Based Sensing Device for Cardiovascular Disease Patient Management

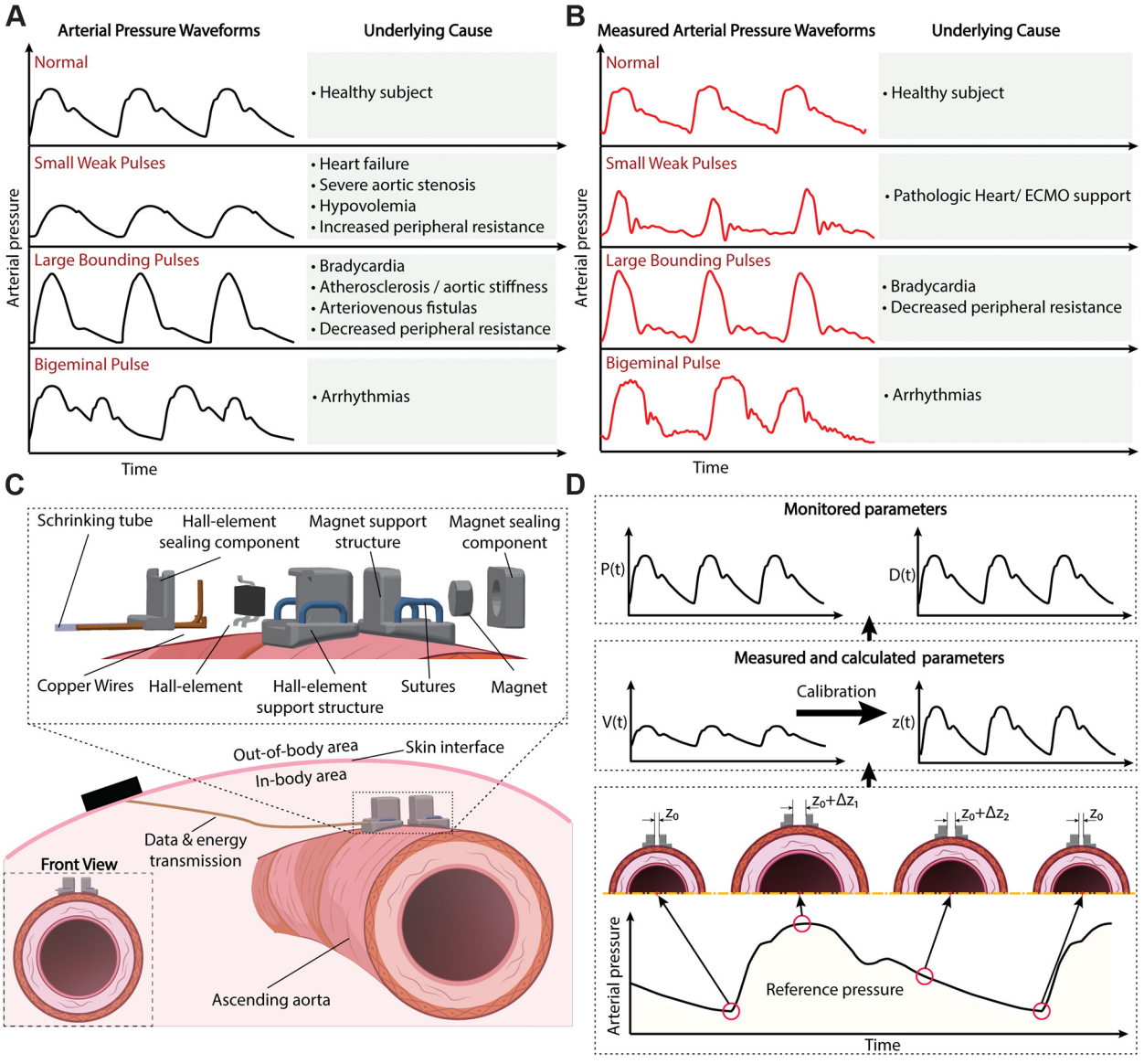

(A) Schematic of the most common cardiovascular diseases and their influence on the blood pressure (BP) waveform. The analysis of the BP waveform contains significant information, which could be used to guide the treatment. **(B)** BP waveforms captured with the sensing device during the in vivo validation. **(C)** Illustration of the hall-based sensing device attachment and a detailed view showing the components comprising the sensing device. The hall-effect sensor (HES) and magnet are completely separated, and they are sutured at a predefined distance on the outer arterial wall. **(D)** The contraction of the heart creates a pulsating pressure profile [P(t)] that travels through the arterial vessels. Depending on the vascular compliance, this pulsating pressure results in a varying vessel diameter [D(t)], which changes the position of the 2 sensing components. During systole, the distance between the components increases, resulting in a weakened magnetic flux at the measurement surface of the HES and, hence, an increased voltage output [V(t)] (negative sensitivity selected for the HES). The voltage variation is translated to distance changes [z(t)] via the operation map produced during the calibration of the sensor. The distance between the sensing components is used to deduce the arterial diameter, the arterial circumferential strain and the pressure waveforms in a continuous manner. ECMO = extracorporeal membrane oxygenation.

measurements of the entire ABP waveform, their long-term usage is still complicated by drift, a phenomenon of changing sensor output over time, and the need of a tight fixation on the circumference of the aortic wall, which may lead to unwanted interference with vascular movement and compliance.

Noninvasive measurement of the ABP by cuff-type sphygmomanometer or wearable devices that are

directly attached to the skin provide only incremental values.[21-26] Although the wearable devices have significantly improved the stability of the sensing device, the measurement accuracy and reproducibility are highly affected by body posture, by movement of the measuring device during use, and often by increased ABP at the time of measurement at the clinic (ie, white coat hypertension).[27] Additionally, these devices typically estimate the ABP by using the peripheral blood pressure and generalized mathematical models that are associated with high inaccuracies[28,29] and, hence, can increase the risk of potential misdiagnosis and mistreatment.[11]

We present an improved invasive sensing approach for continuous monitoring of ABP as well as arterial wall diameter (AD) and arterial circumferential strain (ACS). The waveforms of the latter variables constitute the basis to further deduce pulse wave velocity, respiration frequency, and duration of the systolic phase of the cardiac cycle, which can offer new capabilities in CVD treatment management. In detail, similar to the work of Ruhhammer et al,[18] an extravascular sensing device is proposed, which is attached to the outer vascular wall. The device comprises a magnetic flux sensor (hall-effect sensor [HES]) and a miniature magnet, both fully encapsulated in 3-dimensional (3D)-printed biocompatible housings. By eliminating the elastic interconnection between the HES and magnet assemblies, the sensing device avoids not only vascular restriction, but also unwanted drift phenomena. The performance of the hall-based sensing device (HBSD) was first evaluated in vitro using an artificial silicone artery. As a next step, in a proof-of-concept study, the translational capabilities of the HBSD were validated in vivo. In detail, the HBSD was tested in a porcine model under physiologic and pathologic hemodynamic conditions, demonstrating high accuracy in monitoring the ABP and the vascular properties in all experimental settings.

METHODS

DESIGN AND FABRICATION. The proposed HBSD sensor is an extravascular sensing system that enables continuous measurement of the ABP, AD, and ACS. The sensor has been optimized to allow the acquisition of changes in the diameter of large vessels such as the ascending aorta (diameter of 27.2-36.6 mm); however, its parametric design would also allow the adaptation of the sensor to function accurately even when smaller vessels (minimum diameter of 10 mm) need to be monitored. The sensing approach and the device structure are presented in **Figures 1C and 1D**. In short, the device consists of 2 distinct components, namely the magnet component and the HES component, which are attached to the outer wall of the aorta. With no physical interconnection of the components, any vessel constriction and restrain is avoided, while, at the same time, drift phenomena due to material fatigue are eliminated.

The fabrication procedure of the HBSD is presented in more detail in Supplemental Appendix 2 as well as in Supplemental Figure 2, while in Supplemental Appendix 8 the considerations for the material selection can be found. Briefly, the magnetic component embodied a miniature nickel-plated, neodymium (N48) permanent magnet (diameter = 2.0 ± 0.1 mm, height = 1.0 ± 0.1 mm, weight = 0.024 g), which was coated with Parylene-C by chemical vapor deposition to improve the temperature stability, as well as to ensure chemical and moisture resistance. For the HES component, an analog-bipolar HES with a SOT-23 packaging and a sensitivity of −45 mV/mT was selected (length × height × thickness = 2.92 mm × 1.30 mm × 1.15 mm, weight = 0.30 ± 0.01 g). Both components were encapsulated in 3D-printed and ultraviolet (UV)-cured housings made of class I biocompatible resin, which enabled exact positioning of the components on the arterial wall. The encapsulated assemblies, along with the copper wires for energy and data transmission, were coated with a 3-μm layer of Parylene-C via chemical vapor deposition to ensure adequate insulation and biocompatibility. By accounting both components of the HBSD, the total weight was 1.38 ± 0.02 g, the height was 3.22 ± 0.01 mm, and the footprint on the vessel wall was 7.00 ± 0.02 mm × 8.00 ± 0.40 mm (longitudinal length × circumferential length). The weight distribution of the HBSD on the aortic wall is given in a qualitative form in Supplemental Figure 9.

WORKING PRINCIPLE. The pulsatile nature of the native heart results in a pulsatile blood flow and, hence, the aorta experiences an altering diameter within each cardiac cycle. As illustrated in **Figure 1D**, the variation in the AD results in a varying distance between the magnet component and the HES component of the sensing device. Hence, a varying magnetic field is applied on the HES and, consequently, a varying output voltage is measured. By measuring the voltage output of the HES, the AD, ACS, and ABP are calculated. Based on the ABP waveform, the respiration frequency and the systolic period of the cardiac cycle can be deduced. When a second sensing device is implanted in the proximity

JACC: BASIC TO TRANSLATIONAL SCIENCE VOL. 8, NO. 5, 2023
MAY 2023:546-564

of the first sensor, the pulse wave velocity (PWV) can also be measured.

A thorough description of the steps required to obtain the aforementioned properties is given in **Figure 2**. Specifically, the deduction of the AD is based on the working principle of the HES because the latter responds linearly to the magnetic flux induced perpendicular to the measurement surface. Any translation of the permanent magnet results in alterations of the magnetic flux sensed by the HES and, hence, an alteration in the measured voltage output. Based on the predefined and constant sensitivity (S) of the HES, the applied magnetic flux perpendicular to the measuring surface (B_z) can be calculated by the measured output voltage (V_m):

$$B_z = \frac{V_m}{S}(Tesla) \tag{1}$$

By using the "current model" for the analysis of a permanent magnet polarized along its symmetry axis with a uniform magnetization M_s (Supplemental Appendix 1, Supplemental Figure 1),[30] the distance between the centers of the magnet component and the HES component of the sensing device can be calculated from the magnetic flux. This approach results in highly accurate calculation of the distance and accounts for any misalignment between the centers of the components induced by the imprecision of the implantation. However, misalignment induced during the manufacturing process, or any inherent deviation in the residual flux density of the permanent magnet, could drastically deteriorate the accuracy of the mathematically calculated distance. To eliminate the risk for inaccuracies, we conducted a calibration procedure for each sensing device (Supplemental Appendix 6). Based on the calibration procedure, the voltage output to distance relation was acquired for all possible orientations and misalignments of the sensing components (**Figure 2A**), resulting in a "calibration space" for each sensing device (**Figure 2C**). This calibration space is defined by second-order exponential equations:

$$z(t) = a \cdot e^{b \cdot V_m(t)} + c \cdot e^{d \cdot V_m(t)} \quad (mm)$$
$$with\ a, b, c, d \equiv f(\varphi, \gamma, r) \tag{2}$$

where z is the distance between the center of the magnet component and the HES component, t is the time index, φ is the misalignment angle in the yaw plane, γ is the misalignment angle in the pitch plane, r is the misalignment of the magnet and HES centers in the x-y plane expressed as a radius, and V_m is the measured voltage output. a, b, c, and d are exponential coefficients that depend on the misalignment parameters.

In **Figure 2D**, the usage of the calibration space and the necessary steps to derive the monitored variables are depicted. More precisely, during the implantation procedure of the sensing device, the misalignment angles φ and γ and the misalignment radius r are measured. These quantities are then set as input parameters in the calibration space to acquire the appropriate voltage output to distance relation, termed the operating map. In case the measured values of φ, γ, and r do not coincide with the calibration values, a spline-based multivariate interpolation is conducted. As a next step, based on **Figure 2B**, the AD can be calculated directly from the distance between the magnet component and the HES component by

$$D(t) = D_0 + \frac{z(t) - z_0}{\sin(k/2)} \ (mm) \tag{3}$$

where $z(t)$ is the distance between the magnet component and the HES component calculated by equation 2, z_0 is the initial distance between the magnet component and the HES component, k is the angle between the magnet component and the HES component with respect to the center of the aorta in the x-y plane, and D_0 is the initial aortic diameter.

The circumferential arterial strain can be calculated from the arterial diameter as:

$$\varepsilon_c = \frac{D(t) - D_0}{D_0} \tag{4}$$

The calculation of the ABP is based on the Young-Laplace equation defined for thin-walled vessels,[31] given as

$$\sigma_c = P\frac{R}{\delta} \tag{5}$$

with σ_c being the circumferential stress, P being the arterial pressure, R being the arterial wall radius, and δ being the arterial wall thickness. When the arterial wall is considered as nonviscous and inertialess material with a linear elastic response, the circumferential stress is linearly related to the strain ε_c with the elastic Young modulus E_Y ($\sigma_c = E_Y\varepsilon_c$). However, studies have shown that the arterial wall is characterized by a viscoelastic behavior.[10] In this work, the viscoelastic behavior of the arterial wall is taken into consideration by incorporating the effect of the rate of change of strain in the stress-strain

FIGURE 2 **Working Principle and Characterization of the HBSD**

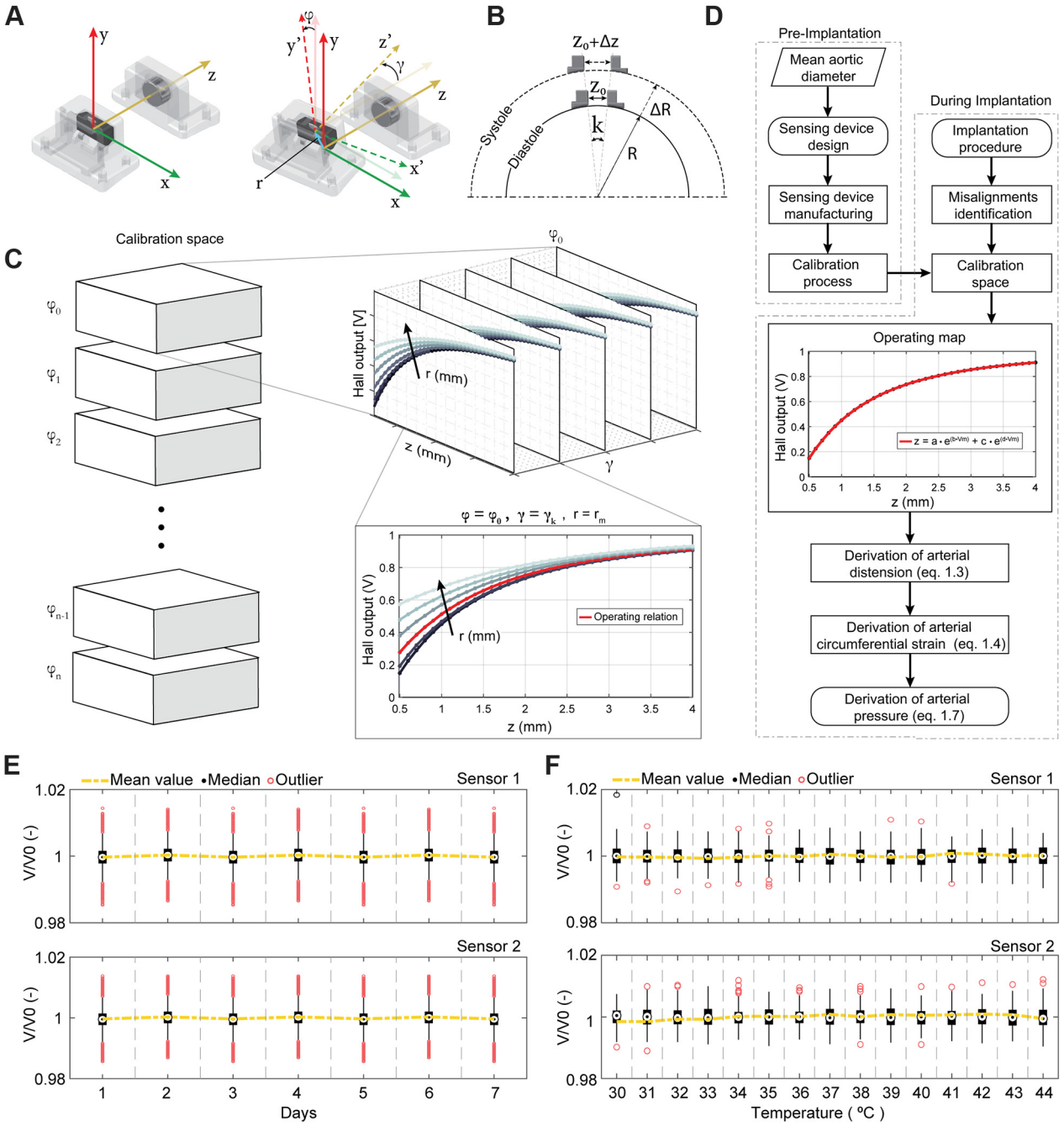

(A) Misalignment between the centers of the sensing components during the implantation procedure. φ is the angle in the yaw plane ($x' - y'$), γ is the angle in the pitch plane ($x' - z'$), and r is the misalignment of the magnet and hall-effect sensor (HES) centers in the yaw plane expressed as a radius. **(B)** Schematic of the changing distance between the sensing components within a cardiac cycle. z_0 is the initial distance between the magnet component and the HES component, k is the angle between the magnet and the HES with respect to the center of the aorta in the yaw plane, and R is the arterial radius during diastole, while Δ R and Δ z are the change in arterial radius and distance, respectively. **(C)** Each hall-based sensing device (HBSD) is calibrated for a set of φ, γ, and r combinations, resulting on the depicted calibration space. The measured misalignment values are used as driving parameters in the calibration space to identify the operating relation between the sensor output and the distance between the sensing components. **(D)** Flowchart of the steps necessary to derive the arterial distension, arterial circumferential strain, and arterial blood pressure. **(E)** HBSDs evaluated for their operation robustness when they are immersed in a 0.9% saline bath at 37 °C for 7 days. Both sensors show great stability, with the change in their response being within the initial deviation of the sensor. **(F)** The performance of 2 sensors was evaluated in a temperature ramp test. Temperature changes within the range of 30 °C to 44 °C had no effect on the sensor's response.

relation, as proposed by Peterson et al[32] and given by

$$\sigma_c = E\varepsilon_c + R_m\frac{d\varepsilon_c}{dt} \quad (6)$$

By substituting equation 6 to 1, the arterial pressure is calculated by

$$P = \frac{\delta}{R}\left(E\varepsilon_c + R_m\frac{d\varepsilon_c}{dt}\right) \quad (7)$$

with E and R_m being subject-specific elastic moduli that are identified with in situ calibration during the implantation process.

The respiratory activity influences the transmural pressure (pressure inside the heart chamber minus the intrapleural pressure), resulting in increased or decreased preload and ventricular stroke volume during inspiration or expiration, respectively. These alterations in preload and stroke volume during the respiration cycles affect the ABP, allowing the deduction of the respiratory frequency by the ABP waveform. The latter deduction requires accurate identification of the onset of each cardiac cycle. In this study, we identified the cardiac cycle onsets based on the maxima of the first derivative of the ABP waveform, when the latter is low-pass filtered with an 18th-order, zero-phase finite impulse response filter with a cutoff frequency of 8 Hz (Supplemental Appendix 3, Supplemental Figure 3). The cardiac cycle onsets enable the extraction of the systolic pressure (SP). The SP points of the ABP result in a new waveform. By identifying the minima of this waveform, the respiration period can be calculated as the time interval between 2 consecutive minima. Consequently, the respiration frequency is deduced as the inverse of the respiration period. A detailed flowchart of the described process is given in Supplemental Figure 5.

For the calculation of the systolic phase of the cardiac cycle, the cycle onset along with the dicrotic notch are prerequisites. However, the identification of the dicrotic notch is not trivial. In this work, we followed the process described in Supplemental Figure 4. In short, the maxima of the first derivative of the low-pass-filtered ABP waveform, which do not correspond to the cardiac cycle onsets and the index of which exceeds the SP index, are identified. The indexes of these maxima are then used as pivot points to search and identify the regional maxima of the original ABP waveform. The regional maxima correspond to the dicrotic notch of each cardiac cycle. By calculating the time interval between the onset and the dicrotic notch of each cycle, the systolic phase of the cardiac cycle is deduced (Supplemental Figure 4).

The PWV can be measured by attaching a second sensor in the proximity of the first sensor. More precisely, the PWV is calculated by the division of the distance between the 2 sensors and the time interval between the cardiac cycle onset on the first sensor and the same cardiac cycle onset of the second sensor.

CHARACTERIZATION OF HBSD. The HBSD was tested and characterized with respect to its robustness to sterilization, immersion into liquid, temperature changes, dynamic and cyclic loading, as well as with respect to misalignment effects induced by imprecision of the implantation. In detail, 5 HBSDs were sterilized by autoclaving (121 °C for 20 minutes) to ensure their robustness in common sterilization procedures. The autoclaved sensing devices were mounted on a holding structure that ensured a fixed distance between the magnet and the HES components. The holding structure with the sensing devices attached was immersed in a 0.9% saline solution bath that was kept at 37 °C via a heating element (Corio; JULABO GmbH). The sensing devices were directly connected to an NI-DAQ-USB6210 (National Instruments; 1 kHz sampling frequency) and the data were continuously registered in a desktop PC for 7 days. After this period, all sensors were retrieved to be examined for swelling. Based on Dual et al,[8] the weight of each sensor was measured on a precision scale (ALJ 500-4A; KERN & SOHN GmbH). After applying vacuum and heat (100 °C) for 2 hours, the weight of each sensor was measured again on the same precision scale.

The temperature experiments were conducted with the HBSDs (n = 5) being mounted on a holding structure and immersed in a 0.9% saline solution bath. The temperature of the bath ranged from 30 °C to 44 °C in steps of 1 °C, and it was measured with a thermistor (MA-100; Amphenol Advanced Sensors). The response of the sensing devices as well as the temperature of the bath were acquired via an NI-DAQ-USB6210 (National Instruments; 1 kHz sampling frequency). For each temperature setting, after the temperature in the bath had stabilized at the required level, the data were measured and collected in 30-minute windows and registered to a desktop PC.

To evaluate the robustness of the sensing devices in long-term cyclic loading, tests were performed on a tensile testing machine (AGS-X, Shimadzu Schweiz GmbH). The clamping of the sensing devices on the tensile device required specific mountings that have been designed and manufactured out of polylactic acid with fused deposition modeling 3D printing. The cyclic loading emulated the maximum distension of

2 mm that the sensing device could measure when implanted on an ascending aorta with a diameter of 30 mm. The moving velocity was 4 $mm \cdot s^{-1}$, emulating a heart rate of 60 beats/min and symmetric systolic and diastolic periods.

Finally, the assessment of the misalignment effects on the response and accuracy of the HBSD was based on the calibration space developed during the HBSD calibration procedure in Supplemental Appendix 6.

IN VITRO SETUP AND EXPERIMENTS. The performance of the HBSD in measuring the AD, ACS, and ABP was first evaluated in vitro. The test bench for the in vitro tests (shown in **Figure 3A**) consisted of a linear motor (P01-37x120F, NTI AG LinMot & MagSpring), a bellows, 2 unidirectional valves, a waterproof tank made of Plexiglass, an artificial artery molded with RTV3040 silicone, 2 mountings for the artificial artery with pressure measurement ports, 2 pressure sensors (TruWave, Edwards Lifesciences), a laser optical displacement sensor (optoNCDT, Micro-Epsilon Messtechnik GmbH & Co KG), a flow meter (Sonoflow CO.55/190, Sonotec GmbH), a thermistor (MA-100), and a heating element (Corio).

To adequately mimic the typical expansion and pulsatile nature of the native aorta in the ascending region, the artificial artery had an outer diameter of 30 mm (the typical outer diameter of the ascending aorta in adults is 27.2-36.6 mm)[28] and a wall thickness of 2 mm. The silicone artery was fabricated based on the process described by Zimmerman et al.[33] Five HBSDs were attached on the artificial artery with instant adhesive, and the artificial artery was mounted on the testbench to form a closed loop system. During the in vitro experiments, the tank was filled with a physiologic saline solution and the temperature was controlled at 37 °C. The closed loop system was also filled with saline solution; however, its temperature was not controlled. By manipulating the stroke length and the velocity of the linear motor, various sinusoidal pressure curves could be achieved, accounting for different pressure conditions and various physiologic heart rates. The intravascular pressure (measured through the pressure ports before and after the artificial artery) and the displacement of the arterial wall (measured with the laser optical displacement sensor) were used as reference signals for the evaluation of the performance of the HBSDs.

IN VIVO SETUP AND EXPERIMENTS. The feasibility of HBSD and its performance were further assessed in vivo, in a porcine model, mimicking more accurately the environment and the arterial motions encountered under clinical conditions. In addition, to evaluate the translational readiness, the HBSD was tested under physiologic and pathologic hemodynamic conditions, with the latter being mimicked by implementing cardiopulmonary bypass (CPB) support. All experiments were conducted on adult pigs (n = 12; Swiss large white; female; 96.9 ± 8.7 kg body weight) with a diameter of the ascending aorta of 23.4 ± 3.3 mm. The experiments were divided into 3 phases. In detail, the first 4 experiments facilitated the model and device establishment, wherein the design and electronics of the HBSDs were iteratively optimized and the experimental protocol was established. The second phase, comprised 2 experiments, dedicated to the optimization of the physiologic and hemodynamically deviated animal models as well as to the optimization of the overall experimental protocol. Finally, a device validation phase followed, wherein the standardized assessment of the optimized device was performed in 6 animals. The animal housing and all procedures and protocols were performed with the ethical approval of the local committee for experimental animal research (Cantonal Veterinary Office Zurich) under the license number ZH213/2019.

The experimental procedure of the in vivo experiments is shown in **Figures 4A and 4B**. In detail, after the loss of postural reflexes following premedication with ketamine (Ketasol-100 ad us.vet.; Dr. E. Graeub AG; 15 mg/kg), azaperone (Stresnil; Elanco Tiergesundheit AG; 2 mg/kg), and atropine (Atropin 1%; Kantonsapotheke; 0.05 mg/kg), anesthesia was induced by a bolus injection of propofol (Propofol-Lipuro 1%; B. Braun Medical AG; 1-2 mg/kg body weight), and the animals were intubated. Anesthesia was then maintained with 2% to 3% isoflurane and propofol (2-5 mg/kg/h). Amiodarone (Cordarone, Sanofi; 150 mg bolus intravenous) was administered to stabilize the heart rhythm, while administration of buprenorphine (0.01 mg/kg) every 4 hours for the duration of the procedure was included for the pain management.

Once the animal was anesthetized, as it is depicted in **Figures 4A and 4B**, a left thoracotomy was performed to provide access to the ascending and descending aorta. A perivascular flowmeter (T400; Transonic Systems Inc) was implanted at the base of the ascending aorta to provide reference measurements of the cardiac output. Specifically designed paper-stencil representing the sensors' exact footprint was placed at the predetermined site of sensor implantation on the aorta and served as a guide for the precise placement of 5-0 Prolene surgical sutures (Ethicon). Following the suture placement, the needles were cut, and sutures threaded through

FIGURE 3 **In Vitro Setup and Performance Validation of the HBSD**

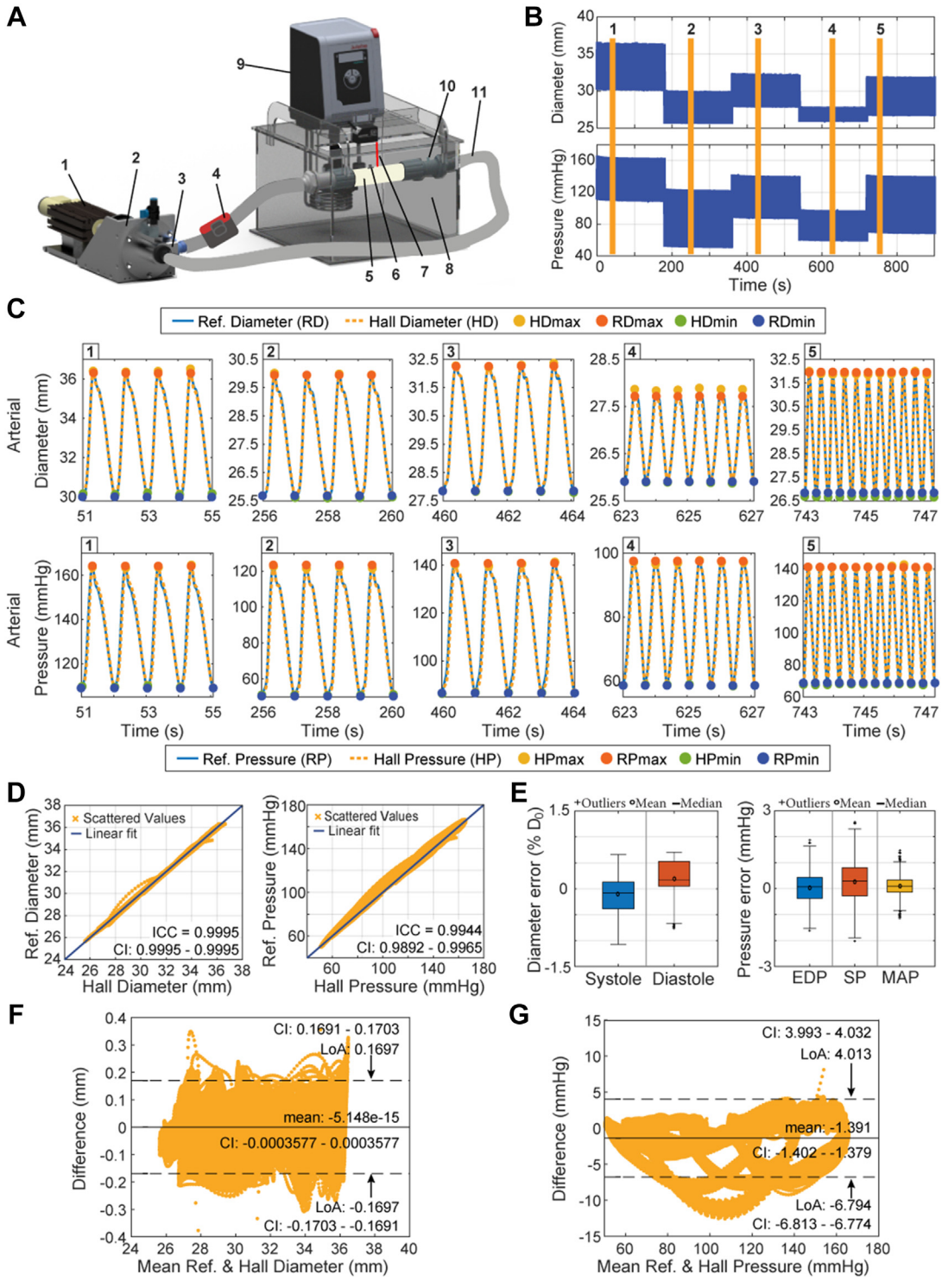

Continued on the next page

prefabricated holes on the HBSD components. The 2 components of each HBSD were then "slided" along their corresponding sutures into the thoracic cavity and then fixed onto the aortic wall by knotting the suture's free ends. The position of the HBSD components was radial (perpendicular to the longitudinal axis of the aortic wall), allowing the distance between the 2 components to freely follow the pulsatile changes of the aortic diameter (the implantation process is demonstrated in Video 1). After fixing the HBSD components, as shown in Supplemental Figure 7, a fluoroscopy image in laterolateral projection was taken and the alignment of the 2 components was assessed. When the HBSD alignment met the acceptance criteria (Supplemental Appendix 7, Supplemental Figure 8), the voltage output of the sensor was measured for 20 seconds, otherwise one of the HBSD components was repositioned and the process was repeated. The mean value of the 20-second measurement was compared with the voltage output identified during the calibration process for the same distance and alignment. In case the voltage deviation exceeded 5% (Supplemental Appendix 7, Supplemental Figure 8), the HBSD was replaced. In a next step, an intravascular fluid-filled blood pressure-measuring catheter (Infiniti 5F PIG 145.038 125 cm; Cordis Corporation) was inserted through the femoral artery and under fluoroscopic guidance carefully positioned at the height of the HBSD at the ascending aorta and connected to a commercial blood pressure sensor to provide the necessary reference signal. All the reference sensors and the HBSDs were connected directly to a data acquisition card, and the data were continuously recorded.

To demonstrate the full capabilities of the HBSD, a number of different hemodynamic conditions were emulated during all animal experiments. Specifically, after a baseline measurement at stable resting conditions, adrenergic stimulation using dobutamine (0.5 mg/mL) was performed to achieve a SP of approximately 130 mm Hg for a prespecified period of 5 minutes. These settings allowed the evaluation of the HBSD under increased blood pressure levels (up to 150 mm Hg) as well as increased heart rates (up to 130 beats/min). Additionally, to investigate the effect of the respiration induced movement on the HBSD performance, 15 to 20 seconds of apnea conditions were conducted.

To test the capabilities of the HBSD in hemodynamic conditions present in patients with heart failure (eg, volume overload) or in case of low pulse pressures (eg, heart failure patients supported with ventricular assist devices), the animals were connected to a CPB circuit. To achieve this, after heparinization (activated clotting time >300 seconds), cannulation of the aortic arch (inflow) and the pulmonary artery (outflow) was performed, and the pig was connected to the CPB circuit (**Figure 4C**). The performance of the HBSD was assessed under various CPB support levels, with and without pharmacological stimulation (dobutamine).

During the in vivo experiments, the intravascular pressure, voltage output of the HBSD, and aortic flow were acquired with an NI-DAQ-USB6210 (2 kHz sampling frequency), driven by a MATLAB 2020b (The MathWorks) script.

On the completion of the study procedure, all animals were euthanized by the administration of an overdose of pentobarbital while still under general anesthesia according to the animal study protocol.

DATA POSTPROCESSING. The data collected during the in vitro and in vivo experiments were filtered with an 18th-order, zero-phase finite impulse response filter with cutoff frequency of 30 Hz and 14 Hz, respectively. Postprocessing was conducted with MATLAB 2020b scripts.

FIGURE 3 Continued

(A) Setup for the in vitro evaluation of the hall-based sensing device (HBSD) comprised: 1) a linear motor; 2) a bellows that enables a volume change; 3) 2 unidirectional valves; 4) a flow meter; 5) an artificial silicone artery; 6) 5 HBSDs; 7) a laser sensor measuring the reference diameter (RD); 8) a waterproof tank; 9) a heating element and a thermometer; 10) a port for reference pressure (RP) measurement; and 11) tubing to circulate the saline solution. **(B)** The applied diameter and pressure conditions to emulate different operating scenarios. In time windows 1 to 3, the heart rate remained at 60 beats/min, with varying loading conditions, while in windows 4 and 5, the heart rate was set to 90 and 160 beats/min, respectively. **(C)** Detailed depiction of the measurements during the operating conditions 1 to 5, shown in panel **B**. The arterial diameter and pressure measured with the HBSD is compared with the RD and RP measurements, while the systolic and diastolic values are presented for all signals. **(D)** Linear association between the diameter measured with the HBSD and the RD, as well as the pressure measured with the HBSD and the RP. The intraclass correlation coefficients for the diameter and pressure measurements were 0.9995 (95% CI: 0.9995-0.9995) and 0.9944 (95% CI: 0.9892-0.9965), respectively. **(E)** Difference of the systolic and diastolic values measured with the HBSD and the reference sensors, including all different operating conditions. The difference in diameter is expressed as a percentage of the initial diastolic aortic diameter. **(F)** Bland-Altman plot of differences between the HBSD and the RD, with the representation of the mean difference, the limits of agreement **(dashed line)** from −1.96 SD to +1.96 SD, and 95% CI. **(G)** Bland-Altman plot of differences between the HBSD and RP, with the representation of the mean difference, the limits of agreement **(dashed line)** from −1.96 SD to +1.96 SD, and 95% CI. EDP = end-diastolic pressure; HP = hall pressure; MAP = mean arterial pressure; SP = systolic pressure.

FIGURE 4 **In Vivo Setup and Performance Validation of the HBSD**

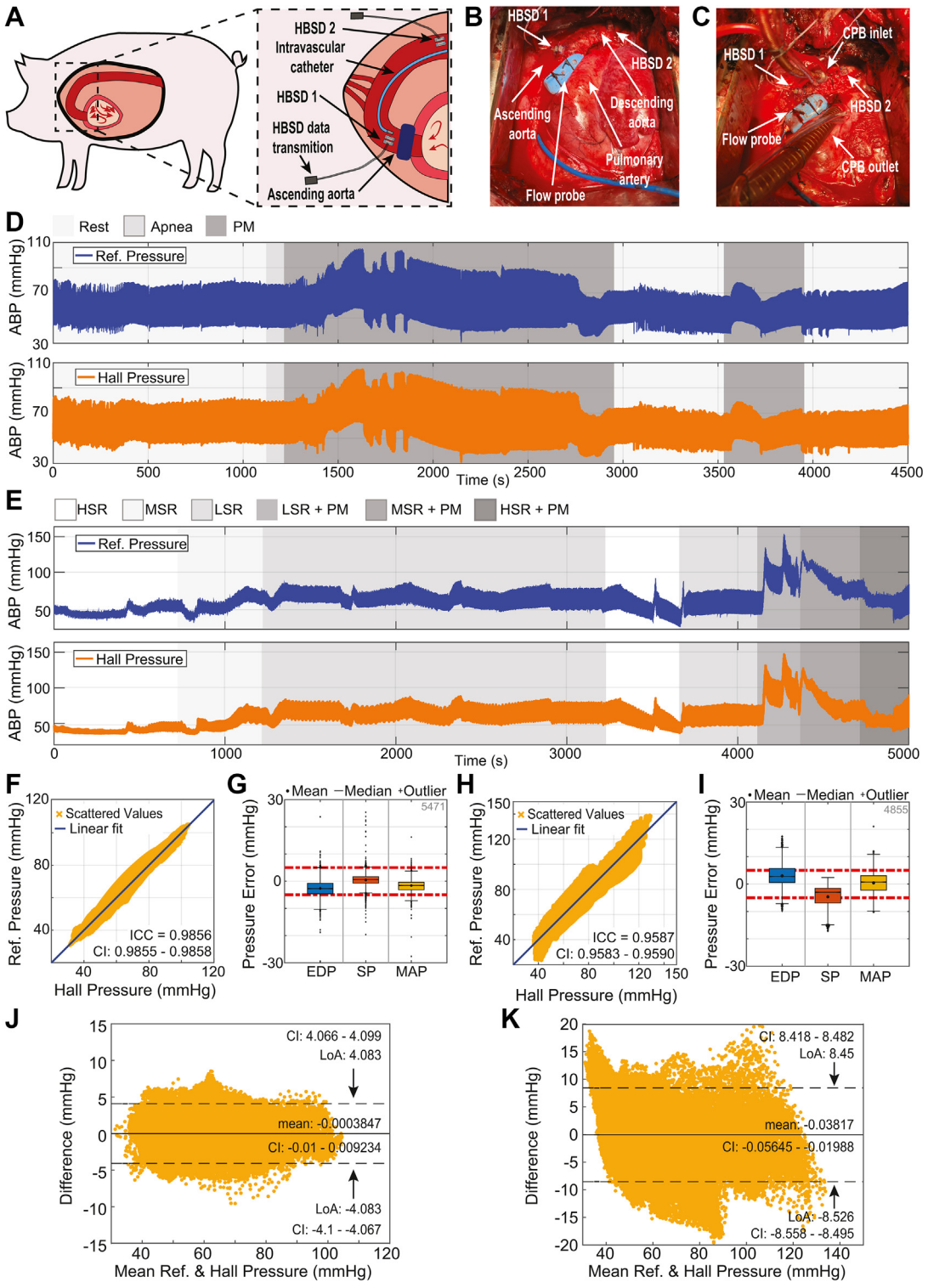

Continued on the next page

STATISTICAL ANALYSIS. The data are presented as time sequences, as well as with the mean ± SD of the difference between the reference measurements and the measurements conducted with the HBSD. The comparison of the reference and HBSD measurement approaches is based on the intraclass correlation coefficient (ICC) with its 95% confidence intervals (CIs), using the model of absolute agreement with single measurements (A-1)[34] implemented by Salarian.[35] Additionally, the data are compared with the Bland-Altman plots of differences with the representation of the mean difference, the limits of agreement from −1.96 SD to +1.96 SD, and 95% CI. All statistical analyses were performed in MATLAB R2020b."

RESULTS

CHARACTERIZATION OF HBSD. The conventional sterilization process, conducted by autoclaving the sensing device at 121 °C for 20 minutes, had no influence on the operation of the hall-effect-based sensor. The response of 2 sensors immersed for 7 days in a physiologic (0.9%) saline solution bath at 37 °C, simulating the environment within the human body, is shown in **Figure 2E**. The change in the mean voltage output (MVO) and the SD with respect to the initial voltage output V0 was infinitesimal over the course of the experiment. Following the immersion in liquid, the sensors were examined for the presence of swelling of the 3D-printed encapsulation structure. Both sensing devices presented a weight increase of <1%.

In **Figure 2F**, the effect of temperature changes on the response of the HBSD are presented, by means of the MVO with respect to the initial voltage output V0. During the ramp-up of the temperature from 30 °C to 44 °C, the MVO was unchanged, while the SD remained in the initial range. This response indicates the robustness of the HBSD to temperature changes in a range much broader than the one expected inside the human body.

The novelty of the proposed HBSD stems from the absence of an elastic interconnecting part between the sensing components. Any elastic component would be prone to cyclic fatigue and, consequently, long-term drift of the sensor. To prove the robust operation of the HBSD over time, long cyclic loading experiments were conducted on a tensile device. As it can be seen in Supplemental Figure 6, the response of the sensor after 30,000 cycles is identical to the initial response, as expected.

In addition, the influence of misalignment among the 2 sensing components of the HBSD, was examined. The response and resolution of the sensor was adequate as long as $\varphi < 2^{\circ}$, $\gamma < 2^{\circ}$ and $r < 0.5$ mm, while the limit in z distance for the investigated design was 2.25 mm. In case the induced misalignments exceed the latter limits, the sensor position needs to be adjusted.

IN VITRO PERFORMANCE VALIDATION. By using the in vitro setup shown in **Figure 3A**, 5 HBSDs were mounted on the surface of the artificial artery (**Figure 3A**), and various physiologic conditions (**Figure 3B**) were emulated by varying the loading range (peak SP ≈30-220 mm Hg) and the heart rate (60-160 beats/min). In **Figure 3C**, a comparison of the diameter measured with the HBSD, and the reference sensor is shown for the applied operating conditions. The profile of the diameter was almost identical to the reference profile in all conditions. Similarly, the pressure profiles acquired with the HBSD indicated high accuracy when compared with the reference pressure profiles (**Figure 3C**). In **Figure 3D**, the linear

FIGURE 4 Continued

(A) Setup for the in vivo evaluation of the HBSD. Under general anesthesia, the ascending aorta was surgically accessed through a left thoracotomy. Further, the 2 components of the HBSD were carefully fixed on the vessel, in a transversal direction, with surgical sutures. Through a femoral access, an intravascular catheter was placed in the ascending aorta to provide the reference pressure values. **(B)** Image of the in vivo setup with HBSD 1 (HS1) and HBSD 2 (HS2) being sutured on the ascending and descending aorta, respectively. The implantation process of one of the sensors is demonstrated in Video 1. **(C)** Image of the in vivo setup after the insertion of the inlet and outlet cardiopulmonary bypass (CPB) tubing. **(D)** Comparison of the arterial blood pressure (ABP) measured via the HBSD and the reference intravascular pigtail catheter during the in vivo experiment. The HBSD was able to accurately capture the varying loading conditions, which were achieved by administering adrenergic medical stimulation. **(E)** Comparison of the ABP measured via the HBSD and the reference intravascular pigtail catheter during the CPB support. The HBSD was able to accurately capture the varying loading conditions, which were achieved by administering boluses of dobutamine and different support ratios. **(F)** The intraclass correlation coefficient for the ABP measured with the HBSD and the reference ABP was 0.9856 (95% CI: 0.9855-0.9858). **(G)** Difference of the EDP, SP, and MAP values measured with the HBSD and the reference sensor, including all different operating conditions. **(H)** The intraclass correlation coefficient for the ABP measured with the HBSD and the reference ABP during the CPB support was 0.9587 (95% CI: 0.9583-0.9590). **(I)** Difference of the EDP, SP, and MAP values measured with the HBSD and the reference sensor, including all different CPB support ratios and pressure conditions. **(J)** Bland-Altman plot of differences between the HBSD and the reference pressure, with the representation of the mean difference, the limits of agreement **(dashed line)** from −1.96 SD to +1.96 SD, and 95% CI. **(K)** Bland-Altman plot of differences between the HBSD and the reference pressure during CPB, with the representation of the mean difference, the limits of agreement **(dashed line)** from −1.96 SD to +1.96 SD, and 95% CIs. HSR = high support ratio; LSR = low support ratio; MSR = medium support ratio; PM = pressure manipulation; other abbreviations as in **Figure 3**.

FIGURE 5 **Cumulative Analysis of HBSD Performance In Vivo, Identification of Cycle Critical Components, and PWV Calculation**

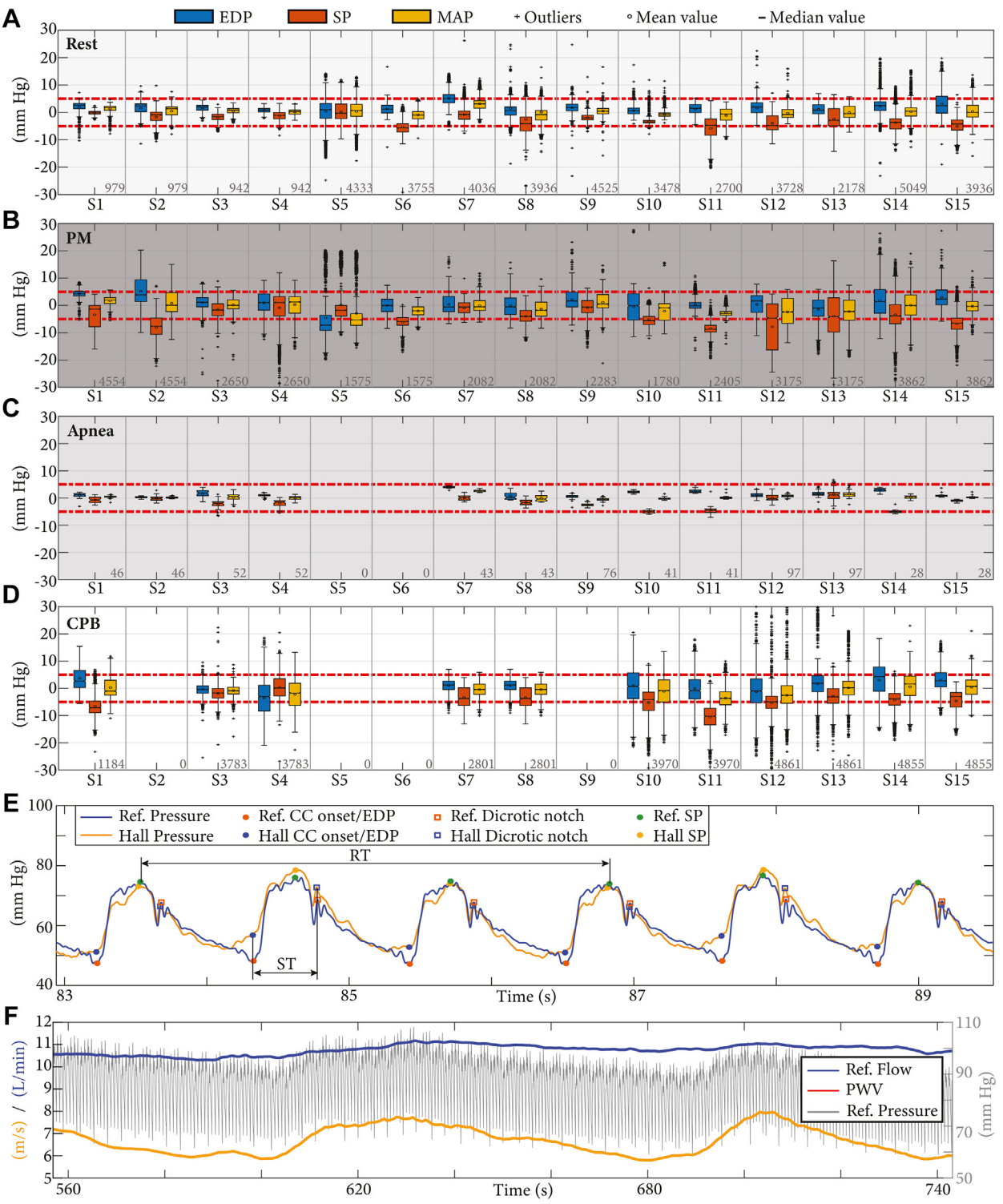

Continued on the next page

association between the reference values and the values measured via the HBSD is illustrated. The ICCs for the diameter and pressure measurements were 0.9995 (95% CI: 0.9995-0.9995) and 0.9944 (95% CI: 0.9892-0.9965), respectively. Although the time-sequence data of diameter and pressure contain crucial information about the condition of a patient, it is of paramount importance to extract the values obtained during systole (SP) and diastole (end-diastolic pressure [EDP]), as well as the mean ABP (mean arterial pressure [MAP]). The mean errors between the reference diameter and the diameter measured via the HBSD, expressed as a percentage of the initial diastolic aortic diameter, were -0.10% ± 0.29% and 0.19% ± 0.34% during diastole and systole, respectively (**Figure 3E**). The mean errors in the EDP, SP, and MAP (**Figure 3E**) were 0.03 ± 0.79 mm Hg, 0.25 ± 0.59 mm Hg, and 0.10 ± 0.38 mm Hg, respectively. Under all conditions examined, the absolute pressure error was below 3 mm Hg. The results of the Bland-Altman plot in **Figure 3F and 3G** also indicate that the HBSD has a mean bias of 0 mm, with limits of agreement (LoA) of 0.16 mm, compared to the reference laser sensor, and a mean bias of −1.39 mm Hg, with LoA of −6.79 to −4.01 mm Hg, compared to the reference pressure sensor.

IN VIVO PERFORMANCE VALIDATION. To demonstrate the full capabilities of the HBSD and assess its translational readiness, an extensive in vivo experimental protocol has been designed and executed in a porcine model. In **Figure 4D**, a comparison of the reference pressure and the pressure measured via the HBSD is illustrated for one of the animal experiments. The pressure signal provided by the HBSD accurately captured the highly varying pressure profiles, regardless of the pressure level and the heart rate. In **Figure 4F**, the linear association between the reference pressure values and the values measured via the HBSD is depicted for the entire experiment. The high association between the 2 measuring approaches is confirmed by the high ICC that was 0.9856 (95% CI: 0.9855-0.9858). The mean errors in the EDP, SP, and MAP (**Figure 4G**) were −2.62 ± 3.17 mm Hg, 0.43 ± 2.39 mm Hg, and −1.60 ± 2.28 mm Hg, respectively. Additionally, in the Bland-Altman plot (**Figure 4J**) it is indicated that the HBSD has a mean bias of 0 mmHg, with LoA of 4.08 mmHg, compared to the reference pressure sensor.

A cumulative analysis of the entire in vivo dataset is provided in **Figures 5A to 5C**. From the 24 sensors implanted in all in vivo experiments, 15 were eligible for further evaluation. The rest of the sensors were excluded due to corrupted reference measurements (2 sensors), animal complications (2 sensors), or sensor malfunction including sensor detachment or wire breakage (5 sensors). In **Figure 5A**, boxplots with the difference between the EDP, SP, and MAP values measured with the HBSDs, and the reference sensors are depicted for stable resting conditions. All sensors demonstrated accurate measurement of EDP, SP, and MAP, with the mean absolute error (MAE) being below 5 mm Hg compared with reference. Overall, HBSDs showed slightly lower accuracy in SP measurements, with increased MAE and SD values. The same boxplots are given in **Figure 5B** for the experimental section in which blood pressure and heart rate stimulation were performed. During these conditions, although all HBSDs demonstrated a MAE below 5 mm Hg in EDP and MAP measurements, 5 HBSDs showed MAE above 5 mm Hg in SP measurement. In addition, during the blood pressure stimulation the SD was increased for all HBSDs. In **Figure 5C**, boxplots of the difference between the EDP, SP, and MAP values measured with the HBSDs and the reference sensors during apnea are depicted. Under apnea, a significant reduction in both MAE and SD is demonstrated for all of the examined HBSDs. However, the sample size (given on the lower right corner of each boxplot) was significantly lower compared with the other sections. Furthermore, for HBSDs 5 and 6, the apnea section was not completed due to animal complications.

In **Figure 4E**, a comparison of the reference pressure and the pressure measured via the HBSD is

FIGURE 5 Continued

Difference of the EDP, SP and MAP values measured with 15 HBSDs and the reference sensor during the in vivo experiments: **(A)** rest/stable animal condition; **(B)** apnea; **(C)** pressure manipulation; **(D)** CPB support. At the **bottom-right corner** of each sensor block, the number of evaluated samples is given. The **patch colors** correspond to those in **Figure 4D**. The **dashed red lines** show the boundaries for pressure measurement device certification. **(E)** Identification of cardiac cycle onset/EDP, dicrotic notch, and SP from the ABP waveform provided from the HBSD and the reference sensor. The systolic phase of the cardiac cycle is calculated as the time interval between the onset and the dicrotic notch of each cardiac cycle. The respiration period and, hence, the respiration frequency are calculated by the time interval between the minimum of the SP values (Supplemental Appendix 3 to 5, Supplemental Figures 3 to 5). **(F)** Pulse wave velocity (PWV) calculation based on the ABP waveforms of 2 consecutive HBSDs. The reference flow and pressure are also depicted to validate the changes in the PWV. CC = cardiac cycle; PM = pressure manipulation; RT = respiration time; ST = systolic phase duration; other abbreviations as in **Figures 3 and 4**.

JACC: BASIC TO TRANSLATIONAL SCIENCE VOL. 8, NO. 5, 2023
MAY 2023:546-564

illustrated during the CPB support. Independent of the pressure level, the CPB support level, and, hence, the effective pulse pressure, the pressure signal provided by the HBSD captured accurately the highly varying pressure profiles. In **Figure 4H**, the linear association between the reference pressure values and the values measured via the HBSD is depicted for the entire experiment under CPB support. The ICC for the ABP measured with the HBSD and the reference ABP during the CPB support was 0.9587 (95% CI: 0.9583-0.9590), confirming the high association between the 2 measuring approaches. The mean errors in the EDP, SP, and MAP (**Figure 4I**) were 3.00 ± 4.75 mm Hg, −4.65 ± 4.40 mm Hg, and 0.46 ± 3.92 mm Hg, respectively. Additionally, in the Bland-Altman plot (**Figure 4K**) it is indicated that during the CPB support, the HBSD has a mean bias of 0.03 mmHg, with LoA of 8.50 mmHg, compared to the reference pressure sensor. In **Figure 5D**, the boxplots showing the difference between the EDP, SP, and MAP values measured with the HBSDs and the reference sensors during the CPB support are illustrated. A total of 11 sensors were assessed during this experimental section, 4 sensors were again excluded due to animal complications or sensor malfunctions (sensor detachment or wire breakage) after the CPB implantation. The examined sensors demonstrated high accuracy in EDP, SP, and MAP measurement regardless of the CPB support level. Except for 2 HBSDs, the analyzed HBSDs showed a MAE lower than 5 mm Hg for all measurement; however, in some cases, the number of outliers has been increased due to misdetections during the identification of the EDP value.

By capturing the entire ABP waveform, as shown in **Figure 5E**, the HBSD enables the identification of the cardiac cycle onsets, EDP, SP, and dicrotic notch through postprocessing. Based on the time index of the dicrotic notch and the onset of a specific cardiac cycle, the systolic phase of the cardiac cycle can be determined. In the same figure, the points used for the calculation of the respiration frequency are showed; however, a detailed flowchart of the calculation is given in the Supplemental Appendix (Supplemental Appendix 5, Supplemental Figure 5). In Supplemental Figure 5, the calculated respiration frequency is compared with the reference respiration frequency, which was set as default value on the ventilator used during the experiments (20 breaths/min).

In **Figure 5F**, the calculated PWV along with the reference flow rate and ABP is illustrated. Although there was not a reference measurement for the PWV, the calculated PWV was in the physiologic range of the animal model used.[29] Additionally, as it is illustrated in **Figure 5F**, the PWV correctly followed the pressure and flow variations, confirming its accuracy.

DISCUSSION

In this work, the design, characterization, and in vitro and in vivo performance of an implantable HBSD for continuous monitoring of ABP, AD, and ACS have been demonstrated under various hemodynamic conditions. The HBSD consists of a HES and a miniature magnet, which are both embedded in 3D-printed biocompatible housings and then coated with Parylene-C. The design of the sensing device allows for optimization of the housings based on the vascular diameter, ensuring safe attachment and accurate measuring capabilities.

The extravascular nature of the HBSD diminishes the risk of thrombosis, blood cell damage and flow obstruction, which constitute common problems that current intravascular sensors encounter.[36] The lack of connective material between the components of the HBSD, along with the minimal footprint and weight (<1.4 g) of the HBSD, ensure that neither relevant restriction on the distension nor gravitational forces due to the device's mass are applied on the arterial wall. Hence, compared with the majority of extravascular sensors that have been proposed for the measurement of vascular and hemodynamic properties,[5-8,16-19] the HBSD may substantially reduce the risk of adverse events.

The robustness of the HBSD was demonstrated during autoclaving procedures, immersion in liquid environment, and temperature changes. Additionally, the sensing device showed excellent response under dynamic cyclic loading. The latter characteristic stems from the avoidance of any elastic connective material, which are prone to fatigue and often the main source of sensor drift. Eliminating drift is a major step toward the achievement of long-term monitoring of CVD patients and constitutes a fundamental benefit compared with the majority of other extravascular or wearable sensing technologies.[37]

The in vitro tests of the HBSD demonstrated its capabilities to monitor the AD, ACS, and ABP. The HBSD was able to accurately capture all applied changes in diameter and pressure of the artificial artery. Comparison of the data produced by the HBSD with the reference data showed high association and agreement, independent of the emulated hemodynamic state. Compared with published data, the

HBSD outperformed the existing extravascular sensing approaches in regards of accuracy.[6,18,20]

The performance of the HBSD was further evaluated in vivo under various hemodynamic conditions (eg, physiologic, pathologic) in a pig model. The pressure waveforms provided by the HBSD demonstrated high association and agreement with the reference pressure waveforms measured by the intravascular catheter during the entire experiment and, independent of the pressure range and the heart rate changes. For the sensors analyzed in this work, the mean error between the EDP, SP, and MAP values provided by the 2 sensing approaches was in all cases significantly smaller than in existing, similar sensing approaches.[18,20] Additionally, the mean error was comparable or smaller than for the only Food and Drug Administration–approved implantable sensor,[38] applicable only in the pulmonary artery.

In 8 of the 12 animals, the hemodynamic conditions were altered by CPB in order to mimic deviation from physiologic hemodynamic properties. In this context, the performance of the HBSD was assessed under low pulse pressure and various loading conditions, similar to those of end-stage heart failure patients supported by ventricular assist devices. The comparison of the ABP waveforms provided by the HBSD demonstrated high association and agreement with the reference pressure waveforms during the entire experiment, independent of the level of CPB support. Considering that the HBSD design was optimized for higher pressure and distension levels, further improvement in the measurement accuracy could be achieved with HBSDs specifically designed for CPB conditions. In this setting, the HBSD could provide the necessary hemodynamic input parameters for the clinical implementation of physiologic control algorithms developed for ventricular assist devices and, hence, improve the performance of such systems and the management of end-stage heart failure patients.[39-41]

In addition, it has been shown that the ABP waveforms captured by HBSD enable the accurate extraction of the cardiac cycle onset/EDP, SP, and dicrotic notch. Based on these quantities, the duration of the systole and the respiration frequency can be calculated. The continuous monitoring of the systolic period of the cardiac cycle can support the calculation of the ejection fraction[42] and, hence, assist in heart failure therapy guidance. Continuous monitoring of the respiration frequency could be used as an input in the prediction of progressive heart failure.[43,44]

The calculation of the PWV when 2 HBSDs are implanted has been also demonstrated. Although there was a lack of reference values during the experiments, the PWV was in physiologic range and followed the pressure and flow rate variations. The acquisition of the PWV could enable the monitoring of biomechanical properties of the vessel that the HBSD is attached and, hence, support the surveillance of CVD patients. In addition, the PWV, combined with the calculated AD, can offer new possibilities for indirect estimation of the cardiac output. The latter could further facilitate the clinical implementation of physiologic control algorithms developed for ventricular assist devices.[39,40,45]

We recognize that the deviation between the HBSD and the reference pressure measurements is higher in the in vivo than in the in vitro experiments, especially in systole. Based on the results obtained during apnea, the main attributor to this discrepancy is the respiration-induced movement of the aortic wall, which was not simulated in vitro. This behavior shows that the HBSD lacks in selectivity and, hence, the measured signal is prone to respiratory artifacts. Although these artifacts can be used to deduce the respiration frequency as described previously, due to the distinct difference between respiration and heart frequency, a correction against these artifacts could be implemented if necessary.

The proper function of HBSD requires highly accurate surgical placement of the 2 sensing components because implantation-induced misalignment can affect the sensing accuracy. Hence, a delivery tool that allows for automatic fixation of the sensing components at predefined positions on the vascular wall and minimizes the invasiveness of the implantation procedure is currently under development. Moreover, data and energy transmission of the presented HBSD was achieved through copper wires. Being aware that this approach may increase the risk of infections at the skin exiting site and device malfunctions, a wireless transmission unit is under development. In this unit, a Bluetooth Low Energy communication protocol is used to transfer data from the sensor to an external receiver. The sensor and the Bluetooth Low Energy module are powered through a rechargeable lithium-ion coin-cell battery, with the battery being recharged every 72 hours through inductive coils. This system is currently being tested in an in vitro setting, and we envision its usage to achieve a fully implantable version of the HBSD with transcutaneous energy and data transmission.

JACC: BASIC TO TRANSLATIONAL SCIENCE VOL. 8, NO. 5, 2023
MAY 2023:546–564

The HBSD in its current design can be exclusively used during open-heart procedures, requiring a sternotomy or lateral thoracotomy for surgical access like left ventricular assist device implantation, coronary artery bypass graft surgery, etc. Hence, considering that the fixation of the sensor requires only routine placement of nonresorbable superficial sutures to the adventitia of the aorta, the implantation of HBSD would not affect greatly the invasiveness of the existing surgical procedures. After such a cardiac surgical procedure, the pericardium is (at least partially) closed and the epicardial fat layer lands itself on top. Within a few weeks after the index procedure, adhesions will be formed between the aorta and the covering layer. These adhesions would possibly lead to sensor encapsulation, which along with the nonresorbable sutures, should enhance the positional stability of the HBSD and render its detachment unlikely. Although the aforementioned encapsulation and the possible vascular scar formation or tissue ingrowth may impact the HBSD's long-term performance, considering that the strength of the magnetic field is not influenced by tissue, the response of the sensor should not be affected. Despite the validation of the HBSD with an extensive in vitro and in vivo experimental protocol, the performance in a closed-chest setting that would allow the assessment of the latter effects, as well as the potential impact during animal movement, has not been investigated yet. In order to evaluate such a scenario and assess long-term device performance, chronic animal trials are planned.

Removal of the current HBSD is not envisioned because the risk of a reoperation for the sensor retrieval would not be justifiable, unless this was mandated in the rare event of a device infection. Hence, in case of a failing sensor, the HBSD would be deactivated, and it would stay inside the body, similar to the process that is currently followed for the CardioMEMS.

We acknowledge also that the changes in the biomechanical properties of the vasculature might affect the relation between the diameter and the pressure over time and, hence, deteriorate the accuracy of the ABP measurements. However, we have shown that a 2-sensor measurement approach enables the PWV derivation, which is highly related with the biomechanical properties.[11,46] We foresee the exploitation of the PWV to implement an online recalibration process.

Finally, it has to be mentioned that although the current hardware implementation is considered sufficient to prove the functionality of the HBSD in an acute setting, the design of the HBSD and the implantation procedure are still in the early developmental phase, and further optimization is necessary to allow its use in humans.

CONCLUSIONS

Continuous measurement of ABP and properties that reflect vascular status have the potential to monitor CVD progression and to closely observe and adjust for the treatment effects of antihypertensive and heart failure medications. This proof-of-concept study provides evidence that the ABP, AD, and ACS waveforms can be accurately and continuously monitored via the proposed sensing approach. Based on the ABP waveform, insights about the PWV, respiration frequency, and systolic phase of the cardiac cycle can be derived. The HBSD demonstrated unaffected performance after sterilization, immersion in liquid, and temperature changes, while it was able to accurately capture the monitored parameters in vitro and in vivo, under various and extreme physiologic and pathologic conditions, induced by CPB support. While the current system requires a cable connection for data and energy transmission, a wireless version with remote monitoring capabilities is currently under development to enable the evaluation of the HBSD in long-term in vivo experiments and allow the translation to the clinical setting.

ACKNOWLEDGMENT The authors thankfully acknowledge Nina Trimmel for her technical assistance during the animal trials.

FUNDING SUPPORT AND AUTHOR DISCLOSURES

This work was supported by the Stavros Niarchos Foundation (SNF). This work is part of the Zurich Heart project under the umbrella of "Hochschulmedizin Zurich." The authors have reported that they have no relationships relevant to the contents of this paper to disclose.

ADDRESS FOR CORRESPONDENCE: Dr Marianne Schmid Daners, Institute for Dynamic Systems and Control, Department of Mechanical and Process Engineering, ETH Zurich, Tannenstrasse 3, CLA G 21.1, 8092 Zurich, Switzerland. E-mail: marischm@ethz.ch. OR Dr Nikola Cesarovic, Translational Cardiovascular Technologies, Department of Health Sciences and Technology, ETH Zurich, Leopold-Ruzicka-Weg 4, HCP H 12.1, 8092 Zürich, Switzerland. E-mail: nikola.cesarovic@hest.ethz.ch.

PERSPECTIVES

COMPETENCY IN PATIENT CARE AND PROCEDURAL SKILLS: Revealing the information hidden in the ABP waveform, as well as other vascular properties, can constitute the cornerstone to allow better patient-compliance surveillance and treatment management in patients experiencing CVDs. In this study, we demonstrate the development and validation of a miniature extravascular hall-based magnetic sensor that allows continuous measurement of the ABP waveform and the waveforms of AD and ACS, allowing to derive also the PWV, respiration frequency, and duration of the systolic phase of the cardiac cycle. Due to the invasiveness of the implantation procedure of the current device, CVD patients following major cardiovascular surgery such as ventricular assist device implantation could benefit the most. However, after improving the data/power transmission and implantation procedure of the device, its usage in the clinical setting and the insights of the measured properties would allow for monitoring disease progression of various CVDs as well as remote monitoring and adjustment of treatment effects.

TRANSLATIONAL OUTLOOK: This proof-of-concept study provides evidence that the proposed HBSD can accurately measure the ABP waveform under various physiologic and pathologic conditions, while it enables the acquisition of various vascular and hemodynamic variables. This is an important initial step to allow the translation of the HBSD toward clinical applications; however, to further enhance the translational capabilities of the HBSD, improvements in device design, data/power transmission, and implantation procedure have to be considered. Finally, prior to testing the feasibility and safety of the HBSD in humans, chronic animal trials are required to investigate the performance of the sensor in a closed-chest environment and to address the consequences of potential tissue ingrowth on the long-term performance of the HBSD.

REFERENCES

1. *Noncommunicable Diseases Country Profiles 2018*. World Health Organization; 2018.

2. Avolio AP, Butlin M, Walsh A. Arterial blood pressure measurement and pulsed wave analysis–their role in enhancing cardiovascular assessment. *Physiol Meas*. 2010;31(1):R1–R47.

3. North BJ, Sinclair DA. The intersection between aging and cardiovascular disease. *Circ Res*. 2012;110(8):1097–1108.

4. Potkay JA. Long term, implantable blood pressure monitoring systems. *Biomed Microdevices*. 2008;10(3):379–392.

5. Lee J, Ihle SJ, Pellegrino GS, et al. Stretchable and suturable fibre sensors for wireless monitoring of connective tissue strain. *Nat Electron*. 2021;4(4):291–301.

6. Lee J, Shin S, Lee S, et al. Highly Sensitive multifilament fiber strain sensors with ultrabroad sensing range for textile electronics. *ACS Nano*. 2018;12(5):4259–4268.

7. Amjadi M, Yoon YJ, Park I. Ultra-stretchable and skin-mountable strain sensors using carbon nanotubes-Ecoflex nanocomposites. *Nanotechnology*. 2015;26(37):375501.

8. Dual SA, Llerena Zambrano B, Sündermann S, et al. Continuous heart volume monitoring by fully implantable soft strain sensor. *Adv Healthc Mater*. 2020;9(19):2000855.

9. Patel AK, Suri HS, Singh J, et al. A review on atherosclerotic biology, wall stiffness, physics of elasticity, and its ultrasound-based measurement. *Curr Atheroscler Rep*. 2016;18(12):83.

10. Guinea GV, Atienza JM, Rojo FJ, et al. Factors influencing the mechanical behaviour of healthy human descending thoracic aorta. *Physiol Meas*. 2010;31(12):1553–1565.

11. Chirinos JA. Arterial Stiffness: Basic Concepts and Measurement Techniques. *J Cardiovasc Transl Res*. 2012;5(3):243–255.

12. McGhee BH, Bridges EJ. Monitoring arterial blood pressure: what you may not know. *Crit Care Nurse*. 2002;22(2):60–79.

13. Bickley L, Szilagyi P. *Bates' Guide to Physical Examination and History Taking*. 12th ed. Wolters Kluwer Health/Lippincott Williams & Wilkins; 2017.

14. Romagnoli S, Ricci Z, Quattrone D, et al. Accuracy of invasive arterial pressure monitoring in cardiovascular patients: an observational study. *Crit Care*. 2014;18(6):644.

15. Bowdle TA. Complications of invasive monitoring. *Anesthesiol Clin North Am*. 2002;20(3):571–588.

16. Shin K-H, Moon C-R, Lee T-H, Lim C-H, Kim Y-J. Flexible wireless pressure sensor module. *Sensors Actuators A Phys*. 2005;123-124:30–35.

17. Boutry CM, Beker L, Kaizawa Y, et al. Biodegradable and flexible arterial-pulse sensor for the wireless monitoring of blood flow. *Nat Biomed Eng*. 2019;3(1):47–57.

18. Ruhhammer J, Herbstritt T, Ruh D, et al. Magnetic sensor for arterial distension and blood pressure monitoring. *Biomed Microdevices*. 2014;16(6):815–827.

19. Zhang T, Ochoa M, Rahimi R, Ziaie B. A wireless, smartphone-aided magnetic strain sensor for biomedical applications. In: *2017 IEEE 30th International Conference on Micro Electro Mechanical Systems (MEMS)*. IEEE; 2017:235–238.

20. Bingger P, Zens M, Woias P. Highly flexible capacitive strain gauge for continuous long-term blood pressure monitoring. *Biomed Microdevices*. 2012;14(3):573–581.

21. Perloff D, Grim C, Flack J, et al. Human blood pressure determination by sphygmomanometry. *Circulation*. 1993;88(5):2460–2470.

22. Wang C, Li X, Hu H, et al. Monitoring of the central blood pressure waveform via a conformal ultrasonic device. *Nat Biomed Eng*. 2018;2(9):687–695.

23. Lipomi DJ, Vosgueritchian M, Tee BC, et al. Skin-like pressure and strain sensors based on transparent elastic films of carbon nanotubes. *Nat Nanotechnol*. 2011;6(12):788–792.

24. Kang S, Lee J, Lee S, et al. Highly sensitive pressure sensor based on bioinspired porous

structure for real-time tactile sensing. *Adv Electron Mater*. 2016;2(12):1600356.

25. Chen LY, Tee BCK, Chortos AL, et al. Continuous wireless pressure monitoring and mapping with ultra-small passive sensors for health monitoring and critical care. *Nat Commun*. 2014;5:5028.

26. Watanabe N, Bando YK, Kawachi T, et al. Development and validation of a novel cuff-less blood pressure monitoring device. *J Am Coll Cardiol Basic Trans Science*. 2017;2(6):631–642.

27. Ogedegbe G, Pickering T. Principles and techniques of blood pressure measurement. *Cardiol Clin*. 2010;28(4):571–586.

28. Morrison TM, Choi G, Zarins CK, Taylor CA. Circumferential and longitudinal cyclic strain of the human thoracic aorta: age-related changes. *Vasc Surg*. 2009;49(4):1029–1036.

29. Kamoi S, Pretty C, Chiew YS, et al. Relationship between stroke volume and pulse wave velocity. *IFAC-PapersOnLine*. 2015;48(20):285–290.

30. Furlani EP. *Permanent Magnet and Electromechanical Devices: Materials, Analysis, and Applications*. 1st ed. Academic Press; 2001.

31. Vlachopoulos C, O'Rourke M, Nichols WW. *McDonald's Blood Flow in Arteries*. 6th ed. CRC Press; 2011.

32. Peterson LH, Jensen RE, Parnell J. Mechanical properties of arteries in vivo. *Circ Res*. 1960;8(3):622–639.

33. Zimmermann JM, Steffen OJ, Vicentini L, et al. Novel augmented physical simulator for the training of transcatheter cardiovascular interventions. *Catheter Cardiovasc Interv*. 2020;95(6):1202–1209.

34. McGraw KO, Wong SP. Forming inferences about some intraclass correlation coefficients. *Psychol Methods*. 1996;1(1):30–46.

35. Salarian A. *Intraclass Correlation Coefficient (ICC)*. MATLAB Central File Exchange; 2022.

36. Yang G-Z. Introduction. In: Yang G-Z, ed. *Implantable Sensors and Systems*. Springer International; 2018:1–17.

37. Yu L, Kim B, Meng E. Chronically implanted pressure sensors: challenges and state of the field. *Sensors*. 2014;14(11):20620–20644.

38. Verdejo HE, Castro PF, Concepción R, et al. Comparison of a radiofrequency-based wireless pressure sensor to Swan-Ganz catheter and echocardiography for ambulatory assessment of pulmonary artery pressure in heart failure. *J Am Coll Cardiol*. 2007;50(25):2375–2382.

39. AlOmari A-HH, Savkin AV, Stevens M, et al. Developments in control systems for rotary left ventricular assist devices for heart failure patients: a review. *Physiol Meas*. 2013;34(1):R1–R27.

40. Petrou A, Monn M, Meboldt M, Schmid Daners M. A novel multi-objective physiological control system for rotary left ventricular assist devices. *Ann Biomed Eng*. 2017;45(12):2899–2910.

41. Abe Y, Chinzei T, Mabuchi K, et al. Physiological control of a total artificial heart: conductance- and arterial pressure-based control. *J Appl Physiol*. 1998;84(3):868–876.

42. Eddleman EE, Swatzell RH, Bancroft WH, Baldone JC, Tucker MS. The use of the systolic time intervals for predicting left ventricular ejection fraction in ischemic heart disease. *Am Heart J*. 1977;93(4):450–454.

43. Baumert M, Linz D, Stone K, et al. Mean nocturnal respiratory rate predicts cardiovascular and all-cause mortality in community-dwelling older men and women. *Eur Respir J*. 2019;54(1):1802175.

44. Goetze S, Zhang Y, An Q, et al. Ambulatory respiratory rate trends identify patients at higher risk of worsening heart failure in implantable cardioverter defibrillator and biventricular device recipients: a novel ambulatory parameter to optimize heart failure management. *J Interv Card Electrophysiol*. 2015;43(1):21–29.

45. Magkoutas K, Arm P, Meboldt M, Schmid Daners M. Physiologic data-driven iterative learning control for left ventricular assist devices. *Front Cardiovasc Med*. 2022;9(3):922387.

46. de Rezende Mikael L, Gomes de Paiva AM, Gomes MM, et al. Vascular aging and arterial stiffness. *Arq Bras Cardiol*. 2017;109(3):253–258.

KEY WORDS arterial distension, arterial strain, blood pressure, CVD monitoring, hall-effect sensor

APPENDIX For expanded Methods and References sections as well as a supplemental table, figures, and a video, please see the online version of this paper.